



Cite this: *J. Mater. Chem. C*, 2021,
9, 2823

Multilayered PtSe₂/pyramid-Si heterostructure array with light confinement effect for high-performance photodetection, image sensing and light trajectory tracking applications†

Mengru Ma,^a Huahan Chen,^a Kunnan Zhou,^a Chao Xie,^{ID} *^a Yi Liang,^a Li Wang,^a Chunyan Wu,^{ID} ^a Wenhua Yang,^a Jiawen Guo^b and Linbao Luo^{ID} *^a

Two-dimensional layered (2D) materials are currently attracting intensive research interest for high-performance photodetection and other optoelectronic applications. However, the study of device integration for multifunctional optoelectronic applications is still at a nascent stage. Here, the assembly of a multilayered PtSe₂/pyramid-Si heterostructure-based photodetector array consisting of 8 × 8 device units is demonstrated. Owing to the pronounced light confinement effect of the heterostructures, the devices present a prominent photovoltaic effect, which enables efficient self-driven photodetection in a broadband wavelength spectrum. The $I_{\text{light}}/I_{\text{dark}}$ ratio, responsivity, external quantum efficiency (EQE) and specific detectivity can attain values as high as 5.51×10^6 , 567 mA W⁻¹, 87% and 1.26×10^{13} jones, respectively, upon 810 nm near-infrared (NIR) light illumination. What is more, benefiting from the large-scale homogeneous material growth technique, the photodetector array exhibits excellent uniformity and repeatability in photoresponse performance with negligible unit-to-unit variation. The above characteristics provide the photodetector array with the capability of recording a simple image produced by NIR illumination and monitoring a moving photonic signal, showing the great possibility for NIR image sensing and light trajectory tracking applications.

Received 4th December 2020,
Accepted 12th January 2021

DOI: 10.1039/d0tc05701k

rsc.li/materials-c

Introduction

Photodetectors, as critical kinds of optoelectronic devices that capture optical signals and convert them into electricity, are fundamental components for many civil and military applications, such as imaging, optical communication, environment monitoring, night vision and security checks.^{1–3} In the past few decades, development of photodetectors based on novel functional materials has drawn extensive attention due to the huge potential for realizing high-performance photodetection as well as the ability to overcome the shortcomings of traditional photodetectors. The explored novel functional materials include zero-dimensional (0D) quantum dots,^{4,5} one-dimensional (1D) nanostructures,^{6,7} two-dimensional (2D) layered materials,^{8,9} organic semiconductors,^{10,11} hybrid

perovskite materials^{12,13} and so on. Among them, 2D transition metal dichalcogenides (TMDs, *e.g.*, MoS₂, MoSe₂, WS₂, WSe₂, *etc.*) have been widely studied recently due to their versatile and appealing electronic and optical characteristics such as high carrier mobility, tunable bandgap, enhanced light absorption efficiency, strong photon-matter interaction, outstanding mechanical flexibility and so on.^{2,8,14} With various material synthetic methods and rational device design, a number of 2D TMD-based photodetectors with exceptional device performance have already been demonstrated so far.^{15–17}

In addition to the above introduced 2D TMDs, the newly explored group-10 TMDs (*e.g.*, PtS₂, PtSe₂, PdSe₂, *etc.*) have also stimulated increasing research interest for their prominent material properties in terms of excellent air stability, high carrier mobility exceeding 1000 cm² V⁻¹ s⁻¹, and layer-dependent modulatable bandgap (0–0.25 eV for their bulk and 1.2–1.75 eV for their monolayers).^{18–20} In particular, the widely tunable bandgap makes the group-10 TMDs extremely attractive for wide band photodetection covering the visible to infrared spectrum.^{21,22} For example, a photoconductor comprising a 10 nm-thick exfoliated PtSe₂ flake is very sensitive to 980 nm near-infrared (NIR) light irradiation, showing a responsivity of 10 mA W⁻¹.¹⁹ By fabricating a few-layered

^a School of Electronic Science and Applied Physics, Hefei University of Technology, Hefei, Anhui 230009, P. R. China. E-mail: chao.xie@hfut.edu.cn, luolb@hfut.edu.cn

^b School of Physics and Engineering and Key Laboratory of Material Physics of Ministry of Education, Zhengzhou University, Zhengzhou, Henan 450052 P. R. China

† Electronic supplementary information (ESI) available: Fig. S1–S8. See DOI: 10.1039/d0tc05701k

PtSe₂-based phototransistor on a h-BN substrate with atomically smooth surface, the responsivity can reach as high as 1560 A W⁻¹ upon visible light illumination.²³ In comparison with photoconductors/phototransistors containing individual components, heterostructure-based photodetectors can potentially offer several advantages:²⁴ (1) improved optical absorption efficiency that is helpful for performance enhancement. (2) Broadened spectral range of optical absorption can enable wide band photodetection. (3) The presence of a built-in electric field accelerating the separation and transport of photocarriers is useful for attaining a faster response speed. (4) A heterojunction photodetector can work at zero bias or reverse bias, which can lower dark current, leading to improved detectivity and maximized sensitivity. (5) The complementary characteristics and advantages of both components may bring some new functionalities. Thereby, very recently, benefiting from the advanced growth methods and deterministic transfer techniques, group-10 TMDs have also been integrated with other semiconductor materials including Si, Ge, GaAs, perovskite materials and other 2D materials to construct heterostructure-based photodetectors.^{25–34} These detectors have already attained a level of competitiveness with commercial semiconductor photodiodes with respect to some photoresponse parameters. For instance, Zeng *et al.* reported a heterostructure photodiode by directly growing a multilayered PdSe₂ film on a Si substrate, which has a responsivity of about 300 mA W⁻¹ and a specific detectivity of 10¹³ jones at 780 nm.²⁶ A NIR photodetector containing multilayered PtSe₂ transferred atop a Ge substrate has achieved a responsivity of about 600 mA W⁻¹ and a specific detectivity of 6.3 × 10¹³ jones, at the 1550 nm telecommunication band.³⁵

However, despite the success in the study of group-10 TMD-based photodetectors, the above introduced photodetectors are mainly composed of individual device units, and device integration for multifunctional optoelectronic uses has not yet been demonstrated. For device integration, large-scale homogeneous growth and precise patterning of photoactive materials are necessary for obtaining favorable device uniformity, intra-device isolation and crosstalk depression between adjacent devices. From this perspective, the widely used mechanical exfoliation technique for preparing 2D layered materials is no longer suitable. Here, we present the assembly of a multilayered PtSe₂/pyramid-Si heterostructure-based photodetector array consisting of 8 × 8 device units for preliminary device integration applications. The photodetector array is fabricated by directly growing patterned PtSe₂ films atop a pyramid-Si substrate using a thermally assisted selenization method with the help of a traditional UV photolithography technique. The pyramidal micro-heterostructures have a strong light confinement effect, which enables efficient utilization of incident photons and therefore a pronounced photovoltaic behavior. As a result, the as-fabricated hybrid devices can function as self-driven photodetectors working in a wide wavelength spectrum. A representative detector has attained a large $I_{\text{light}}/I_{\text{dark}}$ ratio of 5.51 × 10⁶, a decent responsivity of 567 mA W⁻¹, a high EQE of 87% and a respectable specific detectivity of 1.26 × 10¹³ jones, under

810 nm NIR illumination at zero bias. What is more, the device array displays good uniformity and repeatability in performance with minor unit-to-unit variation owing to the special material preparation and device fabrication techniques. Furthermore, by recording a “smile” image produced by NIR irradiation and monitoring a moving light signal, the present photodetector array also demonstrates the potential for use in NIR image sensing and light trajectory tracking applications. Importantly, the proposed fabrication technique is highly compatible with the current complementary metal oxide semiconductor (CMOS) and Si-based photonics technologies. It is believed that our work will provide a facile and reliable avenue for the development of 2D layered material heterostructure-based integrated photodetectors for multifunctional optoelectronic applications.

Experimental

Material preparation and characterization

In this work, a thermal-assisted selenization technique was employed to prepare a multilayered PtSe₂ film.³³ A platinum (Pt) layer with a thickness of 10 nm was firstly evaporated on a Si substrate by using electron beam evaporation. Then, the substrate was placed in the central zone of a tube furnace, on the upstream side of which high-purity selenium (Se) powder (99.99%) was laid. The powder was heated to and maintained at ~225 °C to enable evaporation, and a 50 sccm argon (Ar) gas was employed to drag the evaporated gas towards downstream. Meanwhile, the temperature of the central zone was kept at ~400 °C to allow selenization. After about 1 hour, a multilayered PtSe₂ film with grey appearance was obtained on the substrate. The morphology of the pyramid-Si covered with PtSe₂ was observed by using a field emission SEM (Hitachi, SU8020). The topography of the PtSe₂ layer was studied by using a AFM (Benyuan Nanotech Com, CSPM-4000). An HR Evolution (Horiba Jobin Yvon) Raman spectrometer equipped with a 532 nm laser was employed to record the Raman spectra of the samples. The XPS study was carried out on a monochromatic Al Kα source (1486.6 eV) produced by the XPS system. The absorption spectra of the samples were measured using a Shimadzu UV-2550 UV-vis spectrophotometer. The crystal structure was studied using a TEM instrument (JEOL Model JEM-2100F). The XRD pattern was recorded *via* an X-ray diffractometer (X'Pert PRO MPD).

Device fabrication and analysis

The PtSe₂/pyramid-Si heterostructure-based photodetector array was constructed by the following steps. First, an n-type Si substrate (resistivity: 1–10 Ω cm⁻¹) with a 300 nm thick SiO₂ oxidation layer was ultrasonically cleaned in sequence with acetone, ethanol and deionized (DI) water for 20 minutes. Then, a positive photoresist layer was spin-coated on the substrate, followed by defining 8 × 8 exposed square windows through a UV photolithography process. The size of an individual window is 200 × 200 μm². The SiO₂ layer within the window regions was etched away by immersing the substrate in a BOE etchant for 5 minutes, followed by rinsing in DI water several

times. Afterwards, pyramid-shaped microstructures were fabricated on the exposed Si window regions *via* anisotropic etching in a mixture solution of potassium hydroxide (KOH) (5 wt%) and isopropanol (5 vol%) at 90 °C for 30 minutes. Then, the substrate was immersed in dilute hydrochloric acid (HCl) for 30 minutes to remove residual alkali. A ~ 2 nm Al thin layer was slowly deposited onto the substrate through electron beam evaporation, which was spontaneously oxidized into the AlOx layer (~ 3 nm) in air conditions serving as a passivation layer. After that, 10 nm-thick Pt layers were coated onto the pyramid-Si window array by using UV photolithography and electron beam evaporation processes, and PtSe₂ layers were obtained following the above introduced thermal-assisted selenization technique. Finally, the Ti/Au (2 nm/50 nm) top electrode was deposited on PtSe₂ through additional UV photolithography and electron beam evaporation processes, and the bottom electrode was formed by attaching an indium–gallium (In–Ga) alloy to the rear side of the n-Si substrate. A semiconductor characterization system (4200-SCS, Keithley Co. Ltd) was used for electrical measurements. Laser diodes with different wavelengths (Thorlabs, M265L3, M810L3, M1300L3 and M1550L3) were employed as light sources to perform photoresponse measurements. To study the response speed, a signal generator (Tektronix, TDS2022B) was used to drive the laser diode to generate pulsed light illumination with different frequencies, while the electrical signal was recorded by using an oscilloscope (Tektronix, TDS2012B). For the spectral response study, a lab-built optoelectronic system consisting of a light source (LE-SP-LS-XE) and monochromator (LE-SP-M300) was employed. The light intensity of all light sources was calibrated using a power meter (Thorlabs GmbH., PM 100D) before use. For characterization of the photodetector array, the electrical properties of all device units were recorded separately, and the obtained currents were incorporated into 2D current maps. All measurements were performed under ambient conditions at room temperature.

Theoretical simulation

A lab-built program based on FEM was employed to simulate the electric field distribution of the PtSe₂/pyramid-Si and PtSe₂/planar-Si heterostructures. The *x*-direction period, *y*-direction period, height (*h*) of pyramid-Si, and thickness (*t*) of the PtSe₂ film were set to be 2.5 μm , 2.5 μm , 2 μm , and 35 nm, respectively. The periodic boundary conditions were applied in both *x*- and *y*-directions to simulate an infinite area. Considering the experiment condition, the designed structure is covered by semi-infinite air layer with permittivity of 1. The dielectric constants of Si and PtSe₂ were obtained from previous studies.^{56,57}

Results and discussion

In this work, a multilayered PtSe₂/pyramid-Si heterostructure-based photodetector array was constructed *via* directly growing PtSe₂ films with designed patterns atop a pyramid-Si substrate by using a thermally assisted selenization method.³³ Fig. 1a

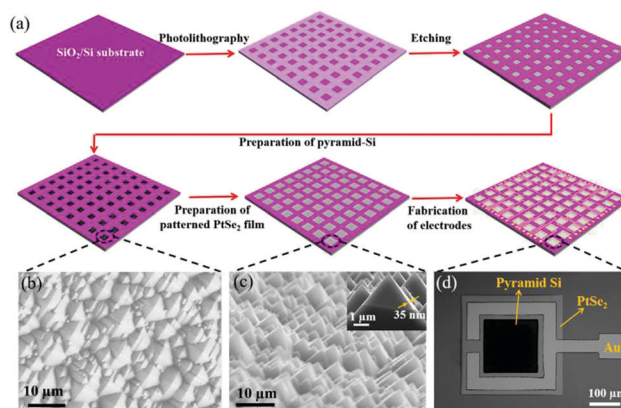


Fig. 1 (a) Schematic illustration of the procedures for constructing the PtSe₂/pyramid-Si heterostructure-based photodetector array. (b) A typical SEM image of pyramid-Si. (c) A cross-sectional SEM image of PtSe₂/pyramid-Si. The inset shows an enlarged SEM image. (d) An optical image of a PtSe₂/pyramid-Si heterostructure-based photodetector.

illustrates the schematic diagram of the fabrication process for the photodetector array, and the details are described in the “Experimental section”. Briefly, 8 × 8 exposed square windows were first defined on a SiO₂/Si substrate covered with a photoresist layer using a photolithography process. After that, the substrate was immersed in a buffered oxide etchant (BOE) solution to remove the SiO₂ layer within the exposed windows. Then, pyramid-Si microstructures were prepared within the window regions by immersing the substrate in an etching solution (Fig. S1a, ESI†).³⁶ Afterwards, with the help of photolithography and electron beam deposition processes, 10 nm Pt films were deposited atop pyramid-Si, which were then converted into PtSe₂ films through a thermal-aided selenization technique (Fig. S1b, ESI†). Finally, the photodetector array was obtained by fabricating Au top and In–Ga bottom electrodes (Fig. S1c, ESI†).

The morphologies of the as-prepared pyramid-Si and the hybrid heterostructure were characterized by scanning electron microscope (SEM) images, as displayed in Fig. 1b and c. It was found that the pyramid-Si was structurally composed of a pyramid-shaped Si microstructure array with a size of several micrometers. This kind of microstructure was responsible for the strong light confinement effect that would be conducive to photoresponse performance improvement, as will be discussed later.³⁶ In addition, the PtSe₂ film with a thickness of ~ 35 nm closely wrapped around the surface of microstructured pyramid-Si. Fig. 1d plots the optical image of a typical as-constructed multilayered PtSe₂/pyramid-Si heterostructure-based photodetector.

The as-grown PtSe₂ film was characterized by X-ray photoemission spectroscopy (XPS) to study its components. As observed in Fig. S2(a) and (b) (ESI†), two distinct peaks corresponding to the Pt 4f_{7/2} and Pt 4f_{5/2} orbitals were situated at 73.28 and 76.63 eV, respectively, while the peaks located at 54.63 and 55.53 eV could be assigned to the Se 3d_{5/2} and Se 3d_{3/2} orbitals of the divalent selenium ions, respectively.³³ In addition, as revealed by the atomic force microscope (AFM)

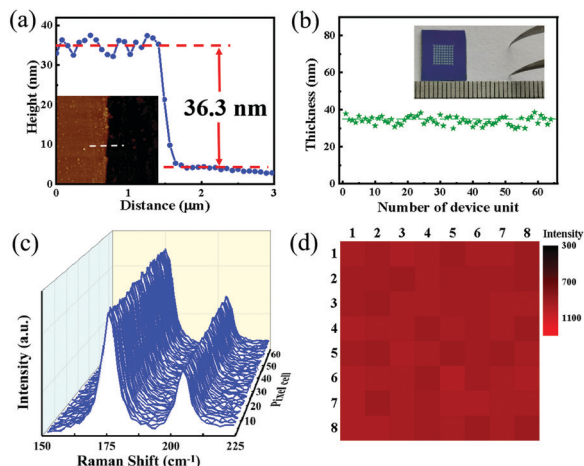


Fig. 2 (a) The height profile of the PtSe₂ layer. The inset shows an AFM image. (b) Statistical distribution of the thickness of the 8 × 8 PtSe₂ patterned films. The inset shows the optical image of the 8 × 8 PtSe₂ patterned films. (c) Raman spectra of individual random spots of the 8 × 8 PtSe₂ patterned films. (d) 2D Raman mapping of the E_g peak extracted from the spectra in (c).

image along with the height profile (Fig. 2a), the thickness of the product was about 36.3 nm, coinciding well with the result observed in the SEM image. Fig. S2(c) (ESI[†]) depicts the X-ray diffraction (XRD) pattern of the film, where four obvious diffraction peaks located at 16.80°, 32.95°, 56.32° and 61.68° due to the (001), (101), (200) and (103) crystal planes of PtSe₂ are observed. Furthermore, the transmission electron microscopy (TEM) image in Fig. S2(d) (ESI[†]) indicates a polycrystalline structure with nanometre-sized crystalline domains of the as-prepared sample. From the high-resolution transmission electron microscopy (HRTEM) image (Fig. S2(e), ESI[†]), the crystalline domain has an interplanar space of *ca.* 0.53 nm, corresponding to the (001) lattice plane of PtSe₂.⁴¹ Furthermore, to probe the material uniformity, an 8 × 8 patterned PtSe₂ film array was directly grown on a SiO₂/Si substrate following the above preparation processes (inset in Fig. 2b). The statistical distribution of the thickness in Fig. 2b discloses a narrow thickness distribution in the range of 30–38 nm with an average value of ~ 34.5 nm for all 64 patterned films. Additionally, the Raman spectra of individual random spots on each patterned film were studied and compared. As plotted in Fig. 2c, two peaks located at 175.44 cm⁻¹ and 204.52 cm⁻¹, corresponding to the E_g in-plane vibrational mode of Se atoms and A_{1g} out-of-plane vibration mode, respectively, could be clearly observed for all spectra.³⁷ The intensity of the E_g peak was extracted from these spectra and summarized by 2D Raman mapping as well (Fig. 2d). Apparently, the intensity of the two representative peaks displayed a very narrow distribution. The above results implied that patterned PtSe₂ film arrays with good quality and uniformity were obtained in our study.

The motivation for designing such a device configuration lies in the outstanding optical characteristics of the PtSe₂/pyramid-Si heterostructure. Fig. 3 illustrates the electric field intensity distribution of the PtSe₂/pyramid-Si heterostructure at

varied cross sections, along with that of the PtSe₂/planar-Si heterostructure, upon 810 nm light illumination, based on the finite element method (FEM). The diameter (*d*) and height (*h*) of the pyramid microstructure were set to be 2.5 and 2 μm, respectively, according to the statistical distribution of both values (Fig. S3, ESI[†]). Apparently, a strong resonantly enhanced electric field could be observed not only inside the pyramid microstructure but also inside the underlying Si substrate for the PtSe₂/pyramid-Si heterostructure. Such a circumstance was in sharp contrast to the PtSe₂/planar-Si heterostructure, where a weak electric field was found (Fig. 3b). The simulation implied a pronounced light confinement and trapping effect in the PtSe₂/pyramid-Si heterostructure, which could enable more incoming photons to be absorbed to produce charge carriers. The above results were reasonable because the pyramid-shaped microstructure array could be regarded as an effective dielectric structure with a gradient refractive index along the negative direction of the *z*-axis. Therefore, the refractive index disparity between free space and bulk Si substrate could be effectively bridged, which led to the excitation of guided mode by the incident light over a wide wavelength spectral regime. The guided mode was likely to be confined at varied sections of the pyramid microstructures, giving high optical absorption and pronounced light–matter interaction.³⁸

To attain a better device performance, a ~ 3 nm AlO_x passivation layer was employed at the PtSe₂/pyramid-Si heterostructure interface, based on our previous report.³⁹ In addition, a control device based on a multilayered PtSe₂/planar-Si heterostructure was also constructed. The electrical and optoelectrical properties of the devices based on the PtSe₂/planar-Si heterostructure, and PtSe₂/pyramid-Si heterostructures with/without the AlO_x passivation layer were first studied and compared in the dark and under 810 nm NIR light irradiation. As displayed in Fig. S4a (ESI[†]), all three heterostructures exhibited an

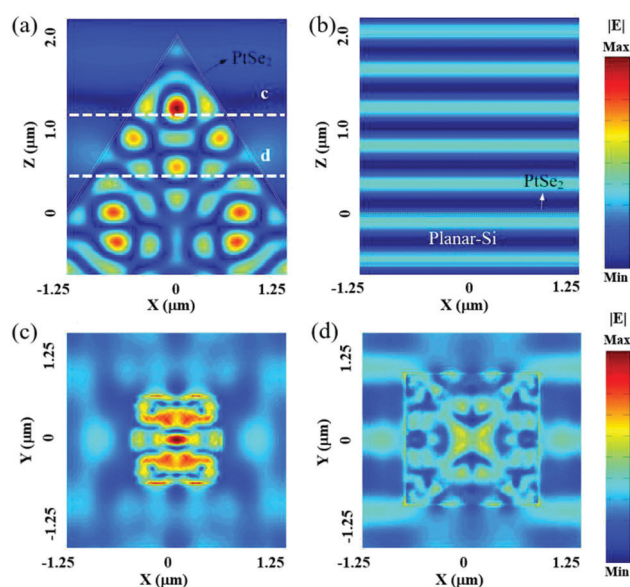


Fig. 3 Simulation of electric field distribution of PtSe₂/pyramid-Si and PtSe₂/planar-Si heterostructures.

apparent current rectifying characteristic in darkness. Interestingly, the device based on the PtSe₂/pyramid-Si heterostructure with the passivation layer had the lowest dark current at both reverse and zero biases (Fig. S4a and b, ESI†). In addition, it was found that this device displayed the most remarkable photo-voltaic behavior as well as the highest photocurrent among the three devices under identical illuminating conditions, as shown in Fig. S4c and d (ESI†). The above characteristics should be ascribed to the following two reasons. AlO_x passivation could greatly suppress the carrier recombination activities at the surface of Si by reducing dangling bonds and defect states, which was beneficial for depressing dark current and improving photocurrent.⁴⁰ Additionally, the pyramid-shaped microstructure array that strongly trapped incident photons could enhance light absorption and induce more photogenerated carriers to participate in the production of photocurrent.³⁶ Therefore, in our study, the PtSe₂/pyramid-Si heterostructure with the AlO_x passivation layer was employed for constructing the photodetector array.

Fig. 4a plots the current–voltage (*I*–*V*) curve of a typical multilayered PtSe₂/pyramid-Si heterostructure with the AlO_x passivation layer on both the linear and semi-logarithmic scales in darkness. An obvious current rectifying characteristic with a large rectification ratio approaching 10⁶ within ±3 V was observed. In consideration of the good ohmic contacts formed between PtSe₂/Au and n-Si/In–Ga,⁴¹ such a diode behavior

should be attributed to the formation of a heterojunction at the PtSe₂/pyramid-Si interface. In addition, the diode ideality factor (*n*) was calculated to be 1.33 by inferring from the ln *I*–*V* curve in the dark (Fig. S5a, ESI†). The low *n* close to the ideal value of 1 revealed a low interface recombination in our heterostructure.⁴² Furthermore, following the thermionic emission theory, the barrier height (ϕ_{BH}) of the heterostructure was calculated to be 880.5 meV (Fig. S5b, ESI†),⁴³ which was larger than that of graphene/Si (450 eV),⁴⁴ sputtered MoS₂/Si (330 meV)⁴⁵ and exfoliated PtSe₂/Si (710 meV)²⁵ heterostructures. The above results suggested that a PtSe₂/pyramid-Si heterostructure with a good diode quality was fabricated. Fig. 4b compares the *I*–*V* curves of the device in the dark and upon 810 nm light irradiation with an intensity of 177.2 mW cm^{−2}. Apparently, the heterostructure exhibited a strong photo-voltaic effect with an open-circuit voltage of 0.39 V and a short-circuit current of 4.1 μA, respectively, giving a photoelectric conversion efficiency of about 0.51%. This kind of characteristic afforded the heterostructure with the ability to work as a self-driven photodetector operating without external electrical energy supply. Furthermore, we studied the time-dependent photoresponse under periodically switched 810 nm NIR illumination. As displayed in Fig. 4c, the heterostructure could be readily turned between a low-current status (~0.8 pA) and a high-current status (~4.3 μA), giving a large *I*_{light}/*I*_{dark} ratio of 5.51 × 10⁶. In addition, our photodetector was also characterized by good reproducibility and air stability. As shown in Fig. 4d and e, after thousands of cycles of operation or 6 months' storage under ambient conditions without any protection, the heterostructure photodetector could still maintain its excellent optoelectronic properties with negligible variation in both photocurrent and dark current.

The above photoresponse characteristics could be correlated with the carrier transport process, as plotted in the energy band diagram of the heterostructure (Fig. 4f). Because of the difference in the work function of n-Si (~4.25 eV for n-Si with a resistivity of 1–10 Ωm^{−1}) and the Fermi level (*E*_F) of multilayered PtSe₂ (~4.84 eV),⁴¹ electrons would diffuse from Si to PtSe₂ to attain thermal equilibrium, as the two components contacted each other. Meanwhile, positively charged empty states would be left within Si to form a depletion region. The charge transfer process would continue until the formation of an aligned Fermi level in the heterostructure. As a consequence, the energy levels within the depletion region bent upward, inducing a built-in electric field at the heterostructure interface. Upon light illumination with the photon energy exceeding the bandgap of Si (*E*_g = 1.12 eV), electron–hole pairs would be produced within and near the depletion region, which were quickly separated by the built-in electric field and collected by electrodes. The above carrier transport processes rendered the production of photocurrent in circuit. On the flipside, upon light irradiation with the photon energy below the bandgap of Si, light absorption taken place within PtSe₂ could excite charge carriers as well. Similar to the internal photoemission process in many metal–semiconductor Schottky junctions,⁴⁶ those electrons with energy higher than the

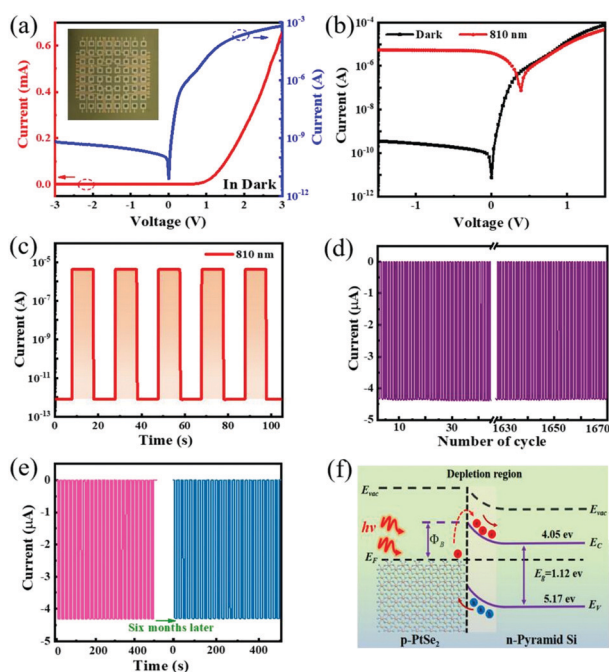


Fig. 4 (a) *I*–*V* curves of a typical PtSe₂/pyramid-Si heterostructure in both linear and semi-logarithmic scales measured in darkness. The inset shows an optical image of an as-fabricated photodetector array. (b) *I*–*V* curves of the heterostructure in the dark and under 810 nm NIR illumination (177.2 mW cm^{−2}). Time-dependent photoresponse of the heterostructure (c) under 810 nm illumination at zero bias, (d) over thousands of cycles of operation, and (e) after 6 months' storage under ambient conditions. (f) Energy band diagram of the heterostructure under illumination at zero bias.

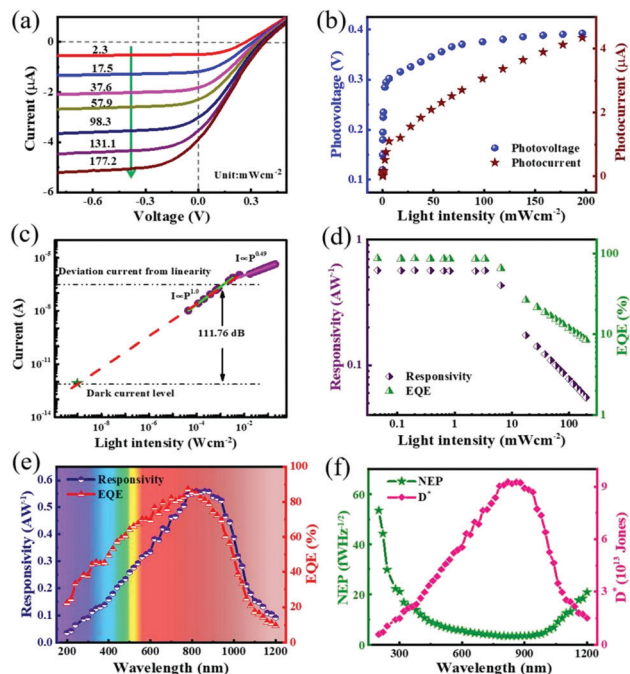


Fig. 5 (a) I - V curves of the heterostructure at different light intensities. (b) Photovoltage and photocurrent as functions of light intensity. (c) The fitting of the curve of photocurrent versus light intensity. (d) Responsivity and EQE as functions of light intensity. (e) Responsivity and EQE as functions of incident light wavelength. (f) NEP and specific detectivity as functions of incident light wavelength.

heterostructure barrier height would surmount the barrier and be injected into the conduction band of Si, ultimately forming the photocurrent.

The light intensity-dependent photoresponse characteristics of the PtSe₂/pyramid-Si heterostructure were further probed. Fig. 5a depicts the I - V curves upon 810 nm NIR light irradiation with varied light intensities from 2.3 to 177.2 mW cm⁻², and the time-dependent photoresponse in a wider light intensity range (0.65–196.3 mW cm⁻²) is provided in Fig. S6a (ESI†). Significantly, both the photovoltage and photocurrent increased monotonously with the increase in light intensity, which was associated with the increased number of photoexcited carriers at an elevated light intensity. From Fig. 5b, it is observed that the values of both photovoltage and photocurrent first exhibited a steep increase in the low light intensity region (0.045–6.36 mW cm⁻²), and then a slow increase in the high light intensity region (6.36–196.3 mW cm⁻²). The photovoltage even displayed a near-saturation behavior when the light intensity exceeded 98.3 mW cm⁻². This kind of feature could be understood from the linearity fitting of the photocurrent versus light intensity curve at different light intensity ranges. Generally, the curve of photocurrent versus light intensity satisfies the relationship $I_{\text{ph}} \propto P^\theta$, where θ denotes an empirical value reflecting the recombination processes of the photogenerated carriers.⁴⁵ As shown in Fig. 5c, by fitting the curve, an ideal value of $\theta = 1 \pm 0.002$ and a non-ideal value of $\theta = 0.49 \pm 0.015$ were attained at the low light intensity range (0.045–3.38 mW cm⁻²) and the high light intensity range (2.3–196.3 mW cm⁻²),

respectively. Therefore, we could conclude that the recombination loss was ignorable in the low light intensity region and it became significant in the high light intensity region.⁴² The nonnegligible recombination loss at the high light intensity range was due to the intensified carrier recombination because of the increased concentration of photogenerated carriers in the heterostructure device.

In addition, the linear dynamic range (LDR) representing the light intensity operating range of a photodetector was studied following the formula $\text{LDR} = 20 \log(I_{\text{ph}}^*/I_{\text{d}})$,⁴⁷ where I_{ph}^* and I_{d} denote the photocurrent at 1 mW cm⁻² light intensity (0.31 μ A) and the dark current (0.8 pA), respectively. Based on the light intensity dependent photoresponse properties (Fig. 5c), the LDR of our heterostructure device was calculated to be 111.76 dB, approaching that of a commercial Si photodiode (120 dB).⁴⁷ The large LDR value implied a low recombination loss in the present device in a certain light intensity region, which was also consistent with the above fitting results.

Next, we calculated two pivotal performance figure-of-merits, *i.e.*, responsivity (R) and external quantum efficiency (EQE), of our heterostructure photodetector. R is described as the ratio of the output photocurrent to the incident light power in the active region of a photodetector and EQE is defined as the ratio of the number of photogenerated electron-hole pairs with contribution to the photocurrent to the number of incident photons. The two parameters are usually described by the following equation:⁴⁸

$$R = \frac{I_{\text{ph}}}{P_{\text{in}}} = \text{EQE} \left(\frac{q\lambda}{hc} \right) G$$

where P_{in} , q , λ , h , c , and G represent the input optical power, elementary charge, wavelength of incident light, Planck's constant, speed of light and photoconductive gain, respectively. The G is 1 in a photodiode-type device lack of an internal gain mechanism.⁸ Therefore, based on our experimental data, the maximum R and EQE values were estimated to be 567 mA W⁻¹ and 87%, respectively, at 810 nm NIR light irradiation with an intensity of 45 μ W cm⁻² at zero bias. Such a relatively large R exceeded that of a multilayered PdSe₂/Si heterostructure (300.2 mA W⁻¹) at zero bias,²⁶ and was comparable to that of graphene/Si heterostructures (435–730 mA W⁻¹)^{42,44} at zero bias and a PtSe₂/Si heterostructure at -2 V bias (490 mA W⁻¹).⁴⁹

Specific detectivity (D^*) and noise equivalent power (NEP) represent the detection limit of a photodetector, and are normally given by⁵⁰

$$D^* = \frac{(AB)^{1/2}}{\text{NEP}}$$

$$\text{NEP} = \frac{\bar{i}_n^{21/2}}{R}$$

where A is the effective device area, B is the bandwidth, and $\bar{i}_n^{21/2}$ is the root-mean-square value of the noise current, respectively. The $\bar{i}_n^{21/2}$ at 1 Hz bandwidth was calculated to be 0.89 fA Hz^{-1/2} for the present photodetector by performing Fourier transformation of the dark current (Fig. S6c and d, ESI†).⁵¹

Table 1 Comparison of key parameters of our device with other reported photodetectors with similar device structures

Device structure	Measurement conditions	$I_{\text{light}}/I_{\text{dark}}$ ratio	R (mA W ⁻¹)	D^* (jones)	τ_r/τ_f (μs)	Ref.
PtSe ₂ /planar-Si	$V^a = -2$ V, white light	—	490	—	—	25
PdSe ₂ /planar-Si	$V = 0$ V, $\lambda = 780$ nm	1.8×10^5	300.2	$\sim 10^{13}$	38/44	26
PtSe ₂ /planar-GaAs	$V = 0$ V, $\lambda = 808$ nm	3×10^4	262	2.52×10^{12}	5.5/6.5	33
PtSe ₂ /planar-Si	$V = 0$ V, $\lambda = 808$ nm	1.5×10^5	520	3.26×10^{13}	55.3/170.5	41
Graphene/planar-Si	$V = 0$ V, $\lambda = 890$ nm	$\sim 10^7$	730	5.77×10^{13}	—	42
Graphene/planar-Si	$V = -2$ V, $\lambda = 850$ –900 nm	$> 10^4$	435	7.69×10^9	$> 10^3$	44
MoS ₂ /planar-Si	$V = 0$ V, $\lambda = 808$ nm	8×10^3	~ 300	$\sim 10^{13}$	3/40	45
PtSe ₂ /pyramid-Si	$V = 0$ V, $\lambda = 810$ nm	5.51×10^6	567	1.26×10^{13}	14.7/17.5	This work

^a V : the operational voltage.

Accordingly, the NEP was deduced to be 1.59×10^{-15} WHz^{-1/2}, which gave a maximum D^* value as high as 1.26×10^{13} jones (cm Hz^{1/2} W⁻¹). Note that the D^* value was comparable to that of many 2D layered material/Si heterostructure photodetectors in previous studies (see Table 1).

The values of R and EQE depended significantly on the incident light intensity as well. As illustrated in Fig. 5d, both values could keep nearly invariant at light intensities below 3.38 mW cm⁻², which again confirmed a linear photoresponse in the low light intensity region. However, they declined rapidly with a further increase in light intensity, which could also be explained by the intensified recombination loss at the higher light intensity. In addition, the $I_{\text{light}}/I_{\text{dark}}$ ratio increased monotonously with increasing light intensity, and reached a maximum value of 5.51×10^6 at a light intensity of 196.3 mW cm⁻² (Fig. S6b, ESI†).

We further characterized the incident light wavelength dependent photoresponse properties of our heterostructure photodetector. Apparently, as seen from Fig. 5e and f, the sensitive behavior was intact over a wide wavelength spectrum from 200 to 1200 nm, signifying the broadband photodetection capability of our device. The photodetector reached the maximum R and D^* and the minimum NEP in its peak response wavelength region of 800–900 nm. What is more, the relatively large EQE in the visible-NIR spectral region (400–1000 nm) suggested an efficient conversion of incident photons to charge carriers. In addition, we also found that our device displayed reliable photoresponse characteristics under 200 nm DUV illumination and even NIR irradiation at 1300 nm and 1550 nm optical communication wavelengths (Fig. S7a–c, ESI†), indicating the possibility for use in DUV light detection and optical communication. The sub-band gap NIR photoresponse was attributed to an internal photon emission process in the PtSe₂/Si heterostructure benefiting from pronounced NIR optical absorption of multilayered PtSe₂ (Fig. S7d, ESI†), as discussed in the analysis of the energy band diagram. Further improvement of DUV and NIR photoresponse is achievable through some strategies such as modification of additional DUV and NIR photoactive media, introducing plasmonic metallic nanostructures resonating in the required spectral regions, as well as integration with optical cavities.^{8,24}

To ascertain the ability to record fast varying optical signals, the response speed of the heterostructure photodetector was then studied. An 810 nm NIR laser diode driven by a function generator was employed as the light source to produce high-frequency light

signals, and a digital oscilloscope was used to record the output photovoltage as a function of time. As depicted in Fig. 6a, the photodetector displayed outstanding switching features with an excellent repeatability to pulsed light with different frequencies of 1, 10 and 25 kHz, suggesting the proper operability of our device in a wide modulation frequency range. In addition, we summarized the relative balance $(V_{\text{max}} - V_{\text{min}})/V_{\text{max}}$ of the photoresponse *versus* the modulation frequency (Fig. 6b). Clearly, the relative balance declined very slowly and it could still maintain 70% of its maximum value at a frequency of 19 kHz. The 3 dB frequency, described as the frequency where the photoresponse drops to 70.7% of its peak value, was estimated to be 19 kHz.⁵² Furthermore, the rise and fall time (τ_r and τ_f) were deduced to be 14.7 and 17.5 μs, respectively, by analyzing a single magnified response curve at 15 kHz (Fig. 6c).⁵³ The fast response speed should be attributed to the good diode quality of the heterostructure with a clean interface (*in situ* material growth) that was conducive to rapid separation/transport of photocarriers and also favourable for depressing trapping/de-trapping of charge carriers due to reduced density of interfacial defects.

To inspect the probability of our PtSe₂/pyramid-Si heterostructure-based photodetector array for use in device integration, the uniformity of the electrical and photoresponse

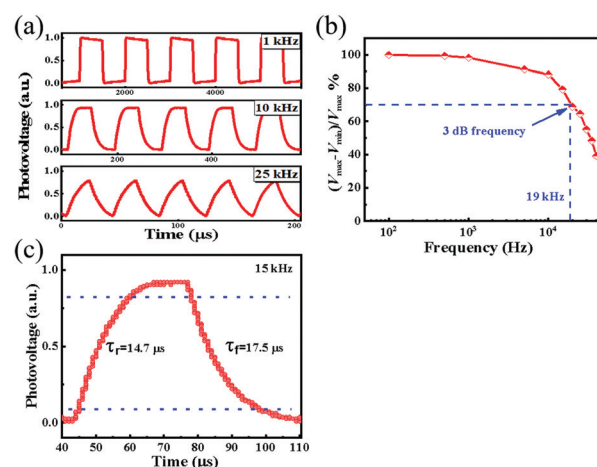


Fig. 6 (a) The transient photoresponse of the heterostructure under pulsed NIR illumination at frequencies of 1 kHz, 10 kHz and 25 kHz. (b) Relative balance $(V_{\text{max}} - V_{\text{min}})/V_{\text{max}}$ as a function of light modulation frequency, showing a 3 dB cutoff frequency of ~ 19 kHz. (c) A single magnified photoresponse for determining the rise/fall times.

characteristics of all 8×8 device units was further characterized. Fig. S8a (ESI†) shows the I - V curves of the 64 devices in darkness and their rectification ratios were extracted and are summarized in Fig. S8b (ESI†). Significantly, all these devices exhibited consistent electrical properties, and the majority had the rectification ratio in the range of 10^5 – 10^6 . Fig. 7a displays the dark current and photocurrent of these devices extracted from the time-dependent photoresponse upon homogeneous 810 nm NIR light illumination (229.6 mW cm^{-2}). To facilitate comparison, the results were summarized in the form of 2D current contrast maps as well (Fig. 7b and c). Apparently, all 64 devices could work properly. Further analysis revealed that they had dark current ranging from 0.7 to 10.7 pA with an average value of 3.87 pA , and photocurrent ranging from 3.87 to $9.73 \text{ }\mu\text{A}$ with an average value of $6.8 \text{ }\mu\text{A}$, at zero bias. Such minor fluctuations in both dark current and photocurrent implied a good uniformity in photoresponse properties. Additionally, the $I_{\text{light}}/I_{\text{dark}}$ ratios plotted in Fig. 7d also showed a narrow fluctuation with the majority in the range of 10^6 – 10^7 . These results revealed that our 8×8 heterostructure-based device units held an outstanding uniformity in device performance, which should be attributed to the good homogeneity of the patterned grown PtSe_2 films as we discussed previously. This feature also enabled a huge potential of our photodetector array for device integration applications.

Furthermore, the capability of our photodetector array to record a NIR light image was presented. Fig. 7e schematically shows the setup for measurement. Homogeneous NIR light irradiation was projected onto the photodetector array, before which a pre-designed shadow mask with a hollow “smile” pattern was placed. Therefore, only device units in the area of the hollow pattern could be illuminated while the others were kept in darkness. The current of all device units was measured separately and the results were described by an 8×8 2D contrast current map. Apparently, as plotted in Fig. 7f, the shape of the “smile” pattern could be distinctly identified with a reasonable spatial resolution, signifying the potential for NIR

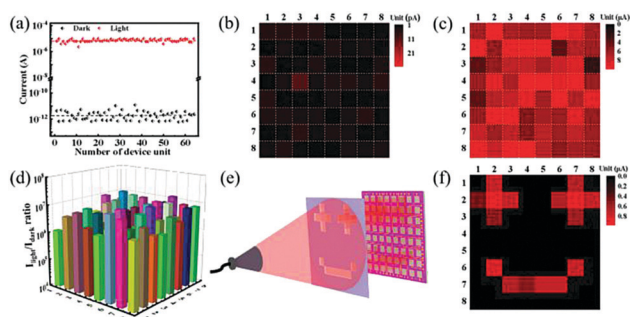


Fig. 7 (a) Current in darkness and under 810 NIR illumination for the 8×8 device units; the dashed lines denote the average values for dark current (black) and photocurrent (red). The 2D current contrast maps showing the current of the 8×8 device units (b) in darkness and (c) upon NIR illumination. (d) 3D diagram of the $I_{\text{light}}/I_{\text{dark}}$ ratio for each device unit. (e) Schematic illustration of the setup for NIR light imaging. (f) The 2D current contrast map of the photodetector array, showing the capability for recording a “smile” image.

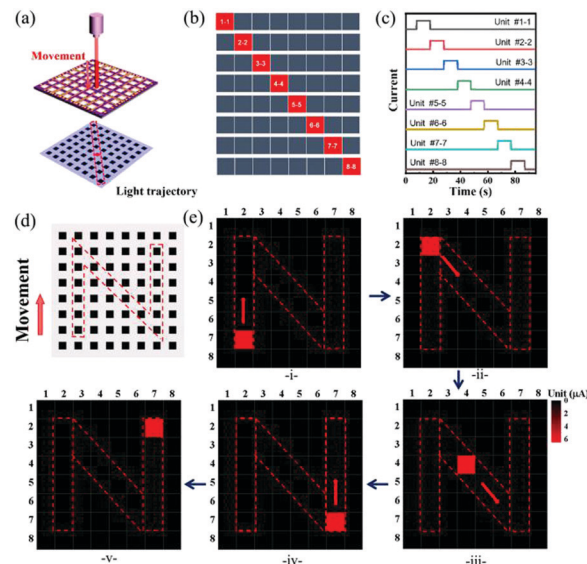


Fig. 8 (a) Schematic illustration of the setup for light trajectory tracking, showing the light spot moving along a straight line. (b) The corresponding light trajectory: from unit 1–1 to unit 8–8. (c) The change of the terminal current when the light spot went through the corresponding device unit. (d) Schematic illustration of the light spot moving along an “N”-shaped trajectory. (e) 2D current contrast maps showing the change of the terminal current when the light spot went through the corresponding device unit.

light image sensing. Further improvement in spatial resolution could be achieved by means of miniaturization of individual devices and/or increasing the density of the device units.

Finally, we demonstrated the device application in light trajectory tracking by using our photodetector array to monitor a rapidly moving object, e.g., a moving NIR light spot. As schematically shown in Fig. 8a and b, when a NIR light source with a small light spot (smaller than the active area of individual device units) moved along a straight line, the light spot would be projected successively on the device unit from unit #1–1 to unit #8–8. Apparently, the terminal current increased significantly when the light spot went through the corresponding device unit while the rest of the device units remained unchanged (Fig. 8c). In addition to the straight line trajectory, our photodetector array could monitor the light spot with more complicated moving trajectories as well. As shown in Fig. 8d, with the light spot moving along an “N”-shaped trajectory, the current of the corresponding device unit increased clearly as observed in the 2D current contrast maps (Fig. 8e), suggesting the capability of recording the motion trajectory of the NIR light spot. Considering the fast response speed, our photodetector array holds great possibility for realizing real-time trajectory tracking of high-speed targets by combining with the real-time data capture and analysis technique.^{54,55}

Conclusions

In summary, we have demonstrated a heterostructure-based 8×8 photodetector array constructed by directly growing

multilayered PtSe₂ patterns atop a pyramid-Si substrate, which possessed the preliminary device integration functionality. The heterostructures displayed a prominent photovoltaic effect due to the strong light confinement behavior, and therefore could operate as self-driven photodetectors in a wide wavelength spectrum. Optoelectronic analysis revealed good photoresponse properties in terms of a large $I_{\text{light}}/I_{\text{dark}}$ ratio of 5.51×10^6 , an eminent responsivity of 567 mA W^{-1} , a high EQE of 87% and a decent specific detectivity of 1.26×10^{13} jones, respectively, upon 810 nm light illumination. In addition, the photodetector array exhibits excellent uniformity and reproducibility in device performance owing to the large-scale homogeneous *in situ* material preparation method. Finally, the device applications in NIR image sensing and light trajectory tracking were presented by using the photodetector array to record a “smile” image projected by NIR light illumination and to monitor a moving NIR optical signal. Benefiting from the high compatibility with the current CMOS and Si-based photonics technologies, the PtSe₂/pyramid-Si heterostructure-based photodetector array will hold great possibility in future NIR integrated optoelectronics with multifunctional application purposes.

Conflicts of interest

There are no conflicts to declare.

Acknowledgements

This work was supported by the National Natural Science Foundation of China (NSFC, No. 51902078, 62074048), the Anhui Provincial Natural Science Foundation (2008085MF205), and the Fundamental Research Funds for the Central Universities (JZ2020HGTB0051, PA2020GDKC0014, JZ2018HGXC0001).

Notes and references

- 1 F. H. L. Koppens, T. Mueller, P. Avouris, A. C. Ferrari, M. S. Vitiello and M. Polini, *Nat. Nanotechnol.*, 2014, **9**, 780–793.
- 2 M. Buscema, J. O. Island, D. J. Groenendijk, S. I. Blanter, G. A. Steele, H. S. J. van der Zant and A. Castellanos-Gomez, *Chem. Soc. Rev.*, 2015, **44**, 3691–3718.
- 3 J. Li, L. Niu, Z. Zheng and F. Yan, *Adv. Mater.*, 2014, **26**, 5239–5273.
- 4 C. Livache, B. Martinez, N. Goubet, C. Gréboval, J. Qu, A. Chu, S. Royer, S. Ithurria, M. G. Silly, B. Dubertret and E. Lhuillier, *Nat. Commun.*, 2019, **10**, 2125.
- 5 G. Konstantatos, M. Badioli, L. Gaudreau, J. Osmond, M. Bernechea, F. P. G. de Arquer, F. Gatti and F. H. L. Koppens, *Nat. Nanotechnol.*, 2012, **7**, 363–368.
- 6 T. Zhai, L. Li, Y. Ma, M. Liao, X. Wang, X. Fang, J. Yao, Y. Bando and D. Golberg, *Chem. Soc. Rev.*, 2011, **40**, 2986–3004.
- 7 J. Jie, W. Zhang, I. Bello, C. S. Lee and S. T. Lee, *Nano Today*, 2010, **5**, 313–336.
- 8 C. Xie, C. Mak, X. Tao and F. Yan, *Adv. Funct. Mater.*, 2017, **27**, 1603886.
- 9 L. Pi, L. Li, K. Liu, Q. Zhang, H. Li and T. Zhai, *Adv. Funct. Mater.*, 2019, **29**, 1904932.
- 10 K.-J. Baeg, M. Binda, D. Natali, M. Caironi and Y.-Y. Noh, *Adv. Mater.*, 2013, **25**, 4267–4295.
- 11 D. Yang and D. Ma, *Adv. Opt. Mater.*, 2019, **7**, 1800522.
- 12 C. Xie, C. Liu, H. Loi and F. Yan, *Adv. Funct. Mater.*, 2020, **30**, 1903907.
- 13 W. Tian, H. Zhou and L. Li, *Small*, 2017, **13**, 1702107.
- 14 J. D. Yao, Z. Q. Zheng and G. W. Yang, *Prog. Mater. Sci.*, 2019, **106**, 100573.
- 15 M. Long, P. Wang, H. Fang and W. Hu, *Adv. Funct. Mater.*, 2019, **29**, 1803807.
- 16 N. Huo and G. Konstantatos, *Adv. Mater.*, 2018, **30**, 1801164.
- 17 J. Yao and G. Yang, *Nanoscale*, 2020, **12**, 454–476.
- 18 Y. Zhao, J. Qiao, P. Yu, Z. Hu, Z. Lin, S. P. Lau, Z. Liu, W. Ji and Y. Chai, *Adv. Mater.*, 2016, **28**, 2399–2407.
- 19 Y. Zhao, J. Qiao, Z. Yu, P. Yu, K. Xu, S. P. Lau, W. Zhou, Z. Liu, X. Wang, W. Ji and Y. Chai, *Adv. Mater.*, 2017, **29**, 1604230.
- 20 W. L. Chow, P. Yu, F. Liu, J. Hong, X. Wang, Q. Zeng, C.-H. Hsu, C. Zhu, J. Zhou, X. Wang, J. Xia, J. Yan, Y. Chen, D. W. T. Yu, Z. Shen, H. Lin, C. Jin, B. K. Tay and Z. Liu, *Adv. Mater.*, 2017, **29**, 1602969.
- 21 X. Yu, P. Yu, D. Wu, B. Singh, Q. Zeng, H. Lin, W. Zhou, J. Lin, K. Suenaga, Z. Liu and Q. J. Wang, *Nat. Commun.*, 2018, **9**, 1545.
- 22 Q. Liang, Q. Wang, Q. Zhang, J. Wei, S. X. Lim, R. Zhu, J. Hu, W. Wei, C. Lee, C. Sow, W. Zhang and A. T. S. Wee, *Adv. Mater.*, 2019, 1807609.
- 23 L. Li, W. Wang, Y. Chai, H. Li, M. Tian and T. Zhai, *Adv. Funct. Mater.*, 2017, **27**, 1701011.
- 24 C. Xie, Y. Wang, Z. X. Zhang, D. Wang and L. B. Luo, *Nano Today*, 2018, **19**, 41–83.
- 25 C. Yim, N. McEvoy, S. Riazimehr, D. S. Schneider, F. Gity, S. Monaghan, P. K. Hurley, M. C. Lemme and G. S. Duesberg, *Nano Lett.*, 2018, **18**, 1794–1800.
- 26 L.-H. Zeng, D. Wu, S.-H. Lin, C. Xie, H.-Y. Yuan, W. Lu, S. P. Lau, Y. Chai, L.-B. Luo, Z.-J. Li and Y. H. Tsang, *Adv. Funct. Mater.*, 2019, **29**, 1806878.
- 27 D. Wu, J. Guo, J. Du, C. Xia, L. Zeng, Y. Tian, Z. Shi, Y. Tian, X. J. Li, Y. H. Tsang and J. Jie, *ACS Nano*, 2019, **13**, 9907–9917.
- 28 L. Luo, D. Wang, C. Xie, J. Hu, X. Zhao and F. Liang, *Adv. Funct. Mater.*, 2019, **29**, 1900849.
- 29 L. Zeng, Q. Chen, Z. Zhang, D. Wu, H. Yuan, Y. Li, W. Qarony, S. P. Lau, L. Luo and Y. H. Tsang, *Adv. Sci.*, 2019, **6**, 1901134.
- 30 Z.-X. Zhang, Long-Hui Zeng, X.-W. Tong, Y. Gao, C. Xie, Y. H. Tsang, L.-B. Luo and Y.-C. Wu, *J. Phys. Chem. Lett.*, 2018, **9**, 1185–1194.
- 31 M. Long, Y. Wang, P. Wang, X. Zhou, H. Xia, C. Luo, S. Huang, G. Zhang, H. Yan, Z. Fan, X. Wu, X. Chen, W. Lu and W. Hu, *ACS Nano*, 2019, **13**, 2511–2519.

- 32 J. Yuan, T. Sun, Z. Hu, W. Yu, W. Ma, K. Zhang, B. Sun, S. P. Lau, Q. Bao, S. Lin and S. Li, *ACS Appl. Mater. Interfaces*, 2018, **10**, 40614–40622.
- 33 L. H. Zeng, S. H. Lin, Z. J. Li, Z. X. Zhang, T. F. Zhang, C. Xie, C. H. Mak, Y. Chai, S. P. Lau, L. B. Luo and Y. H. Tsang, *Adv. Funct. Mater.*, 2018, **28**, 1705970.
- 34 D. Wu, C. Jia, F. Shi, L. Zeng, P. Lin, L. Dong, Z. Shi, Y. Tian, X. Li and J. Jie, *J. Mater. Chem. A*, 2020, **8**, 3632–3642.
- 35 L. Wang, J.-J. Li, Q. Fan, Z.-F. Huang, Y.-C. Lu, C. Xie, C.-Y. Wu and L.-B. Luo, *J. Mater. Chem. C*, 2019, **7**, 5019–5027.
- 36 P. Xiao, J. Mao, K. Ding, W. Luo, W. Hu, X. Zhang, X. Zhang and J. Jie, *Adv. Mater.*, 2018, **30**, 1801729.
- 37 M. O'Brien, N. McEvoy, C. Motta, J.-Y. Zheng, N. C. Berner, J. Kotakoski, K. Elibol, T. J. Pannycook, J. C. Meyer, C. Yim, M. Abid, T. Hallam, J. F. Donegan, S. Sanvito and G. S. Duesberg, *2D Mater.*, 2016, **3**, 021004.
- 38 E. Garnett and P. Yang, *Nano Lett.*, 2010, **10**, 1082–1087.
- 39 J.-Y. Xu, J.-S. Yu, J.-H. Liao, X.-B. Yang, C.-Y. Wu, Y. Wang, L. Wang, C. Xie and L.-B. Luo, *ACS Appl. Mater. Interfaces*, 2019, **11**, 21702–21710.
- 40 L.-B. Luo, H. Hu, X.-H. Wang, R. Lu, Y.-F. Zou, Y.-Q. Yu and F.-X. Liang, *J. Mater. Chem. C*, 2015, **3**, 4723–4728.
- 41 C. Xie, L. Zeng, Z. Zhang, Y. H. Tsang, L. Luo and J. H. Lee, *Nanoscale*, 2018, **10**, 15285–15293.
- 42 X. Li, M. Zhu, M. Du, Z. Lv, L. Zhang, Y. Li, Y. Yang, T. Yang, X. Li, K. Wang, H. Zhu and Y. Fang, *Small*, 2016, **12**, 595–601.
- 43 E. Shi, H. Li, L. Yang, L. Zhang, Z. Li, P. Li, Y. Shang, S. Wu, X. Li, J. Wei, K. Wang, H. Zhu, D. Wu, Y. Fang and A. Cao, *Nano Lett.*, 2013, **13**, 1776–1781.
- 44 X. An, F. Liu, Y. J. Jung and S. Kar, *Nano Lett.*, 2013, **13**, 909–916.
- 45 L. Wang, J. Jie, Z. Shao, Q. Zhang, X. Zhang, Y. Wang, Z. Sun and S.-T. Lee, *Adv. Funct. Mater.*, 2015, **25**, 2910–2919.
- 46 S. M. Sze and K. K. Ng, *Physics of Semiconductor Devices*, 2007.
- 47 X. Gong, M. Tong, Y. Xia, W. Cai, J. S. Moon, Y. Cao, G. Yu, C.-L. Shieh, B. Nilsson and A. J. Heeger, *Science*, 2009, **325**, 1665–1667.
- 48 J. Yao, Z. Zheng and G. Yang, *Adv. Funct. Mater.*, 2017, **27**, 1701823.
- 49 C. Yim, K. Lee, N. McEvoy, M. O'Brien, S. Riazimehr, N. C. Berner, C. P. Cullen, J. Kotakoski, J. C. Meyer, M. C. Lemme and G. S. Duesberg, *ACS Nano*, 2016, **10**, 9550–9558.
- 50 R. Zhuo, L. Zeng, H. Yuan, D. Wu, Y. Wang, Z. Shi, T. Xu, Y. Tian, X. Li and Y. H. Tsang, *Nano Res.*, 2019, **12**, 183–189.
- 51 C. Xie, P. You, Z. Liu, L. Li and F. Yan, *Light: Sci. Appl.*, 2017, **6**, e17023.
- 52 E. Wu, D. Wu, C. Jia, Y. Wang, H. Yuan, L. Zeng, T. Xu, Z. Shi, Y. Tian and X. Li, *ACS Photonics*, 2019, **6**, 565–572.
- 53 L.-H. Zeng, M.-Z. Wang, H. Hu, B. Nie, Y.-Q. Yu, C.-Y. Wu, L. Wang, J.-G. Hu, C. Xie, F.-X. Liang and L.-B. Luo, *ACS Appl. Mater. Interfaces*, 2013, **5**, 9362–9366.
- 54 K. Liu, W. Wang, Y. Yu, X. Hou, Y. Liu, W. Chen, X. Wang, J. Lu and Z. Ni, *Nano Lett.*, 2019, **19**, 8132–8137.
- 55 W. Wu, X. Wang, X. Han, Z. Yang, G. Gao, Y. Zhang, J. Hu, Y. Tan, A. Pan and C. Pan, *Adv. Mater.*, 2019, **31**, 1805913.
- 56 T. K. Chong, J. Wilson, S. Mokkapati and K. R. Catchpole, *J. Opt.*, 2012, **14**, 024012.
- 57 S. Deng, L. Li and Y. Zhang, *ACS Appl. Nano Mater.*, 2018, **1**, 1932–1939.